8

A Method for Optical Proximity Correction of Thermal Processes: Orthogonal Functional Method

Sang-Kon Kim
Hanyang University
South Korea

1. Introduction

Pattern reduction has created a great deal of interest in finding effective methods to reduce the feature sizes of microelectronic and data-storage devices. These methods are divided between top-down approach such as photolithography and bottom-up approach such as self-assembly. For below 32 nm node technology, top-down approach has obstacles such as diffraction-limited resolution and high cost of ownership and bottom-up approach has obstacles such as the insufficient support of processes and mass production.

Thermal treatment is a new process extension technique using current-day lithography equipment and chemically amplified resists (CARs). In the lithography process, thermal processes are softbake (SB), post-exposure bake (PEB), and thermal reflow. The purpose of SB is to remove excess solvent after spin coating, relieve strain in the solid film, and provide better adhesion to the substrate. The purpose of PEB is to reduce the standing wave effect and, thus, increase linewidth control and resolution. The purpose of thermal reflow is to reduce the pattern size by using thermal heating at temperatures about the glass transition temperature of the resist after development. These three kinds of thermal processes are essentially the same for heat treatment, but they have different effects on CD. Hence, it is required to understand mechanism behaviors that drive photo resist image and to deal with optical proximity effects (OPEs) due to thermal processes. OPE is quite severe as the critical dimensions (CDs) shrink down to the sub-30 nm patterns. Although the simulation parameters are not used to analyze the chemical phenomena of thermal processes, the CD bias after thermal reflow can be predicted in the linear system. Through the optical proximity correction (OPC), the distorted image from OPE can be manipulated back to the original design. However, the thermal affects of CD is the non-linear system, so that the prediction of OPE is not easy. Hence, the understanding of mechanistic behaviors that drive photo resist image can make the physically corrected resist model, and achieve the best prediction of resist images across multiple process conditions.

One of the most critical issues for sub-50-nm patterning is patterning a fine contact hole (C/H). The resolution performance of contact hole patterns is lower than that of line and space patterns because the depth of focus (DOF) for patterning contact holes is insufficient due to the low aerial-image contrast. The resist reflow process is a good method due to its simplicity without the additional complex process steps and due to its efficient technique

Source: Lithography, Book edited by: Michael Wang,
ISBN 978-953-307-064-3, pp. 656, February 2010, INTECH, Croatia, downloaded from SCIYO.COM

www.intechopen.com

with the appropriate selection of the resist properties and the thermal loading process conditions. However, it is difficult to predict the results of the thermal flow and the process optimization. Thus, the layout designs are only done by trial and error because there are so many effective parameters, such as baking temperature, baking time, resist original characteristics, resist volume surrounding C/H, initial C/H size and shape, and C/H array. To predict the resist shrinkage of resist reflow, according to the experimental data fitting method, the shrink bias can only be expressed as the functional relationship of the baking temperature, normalized resist volume, and native property of resist. By the quantitative analysis of the shrink bias for the baking temperature, the relationship can be expressed as a linear equation. The simple equation helps in understanding the characteristics of the resist reflow and also shows mechanism for process stabilization.

The objectives of the work presented in this chapter are to make the physically corrected resist model based on the understanding of mechanistic behaviors that drive photo resist image, to achieve the best prediction of resist images across multiple process conditions, and to develop a general simulation approach of OPC to reduce the OPEs during lithography thermal processes. Section 2 describes the modeling of the lithography process, the modeling of thermal processes, and the simulation of those thermal processes. Section 3 describes thermal bias based on the simulation of the models in section 2 and introduces the orthogonal functional method. The simulation results of SB and PEB are used by the comparison of a commercial tool, SOLID-C (Shynopsys Inc.)[1]. Section 4 describes the analysis for the below 45 nm contact hole (C/H) pattern for a KrF 248 nm CAR and 32 nm C/H pattern for a ArF 193 nm CAR. Two stage corrections of model-based OPC are performed by using the orthogonal functional method. Section 5 describes the conclusion of this chapter.

2. Thermal process model

2.1 Simulation benchmarking for the whole resist process

For the semiconductor industry, lithography is the key technology driver and a significant economic factor, currently representing over thirty five percent of the chip manufacturing cost. Significant investments from research and development to device commercialization will improve the infrastructure of this vital technology and maintain industry growth. The cost of experiments is now very large and the complexity of lithographic patterns and processes (e.g. phase shift and chemical amplification) is too big to ignore the simulation. To support this, the availability, accuracy, and easy use of lithography simulation must be improved [2]. As a research tool, lithography simulation performs experiments that would be difficult or impossible to do by any other way.

As a process development and process transfer tool, a simulation tool can quickly evaluate options, optimize processes, or save time and money by reducing the number of experiments in the fab. As a manufacturing tool, it can troubleshoot process problems, determine optimum process settings, and aid in decision making by providing facts to support engineering judgment and intuition. As a learning tool, its proper application allows the user to learn efficiently the lithography process. Hence, performing the physical and molecular simulation can be helpful to analyze, understand, and predict the lithography technologies for gigabit era.

Figure 1 shows the structure of lithography simulation. These simulation models are used for spin coating, soft bake, illumination, exposure, delay, post exposure bake, development,

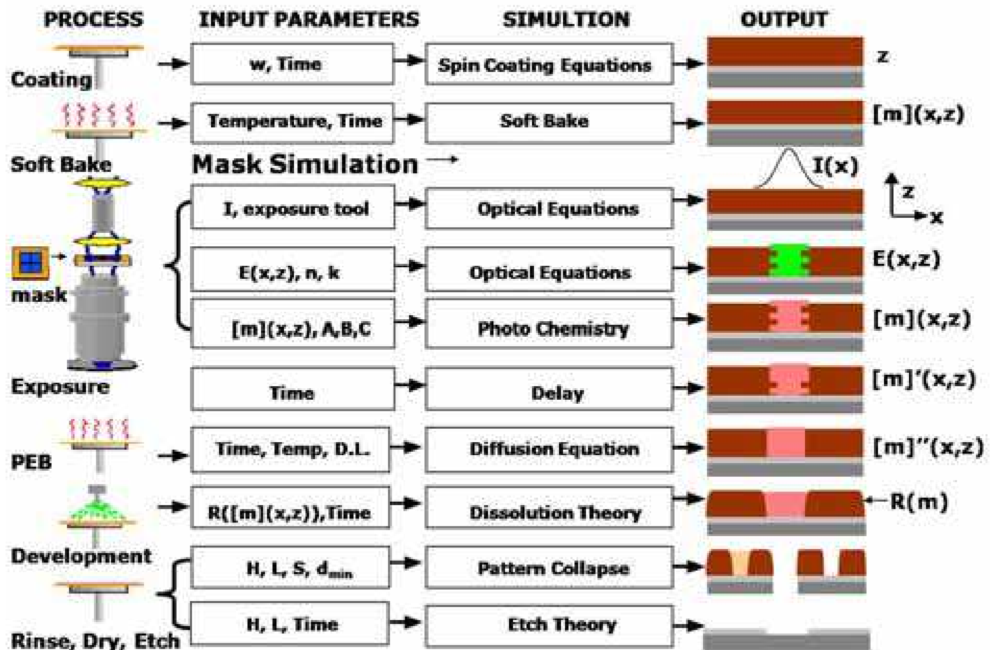

W: spin velocity, I: intensity, E(x,z):exposure, n:refractive index, k:absorbtion index, [m](x,z): photo acid generator (PAG), A, B, C; Dill's parameters, [m]'(x,z): PAG after delay, [m]''(x,z): PAG after PEB, R([m])(x,z): dissolution rate, H: pattern height, L: pattern width, S: line width, d_{min}: minimum line width.

Fig. 1. Simulation modeling

rinse, dry, and etch processes. For the spin coating model, input parameters are spin velocity and time. Resist thickness is calculated by solving the Navier-Stokes equation or the convective diffusion equation. Irregular surfaces caused by spin coating and solvent evaporation are not considered. In the soft bake model, input parameters are temperature and time. The photo acid compound (PAC) is calculated.

The illumination part is modeled as the projection lens system. Aerial image is calculated by solving the optical equations due to illumination parameters as input parameters. In the bulk model, bulk image inside resist is calculated by using the multiple thin layer interference theory and the Berning theory instead of the rigorous solution for the Maxwell's equations. During the exposure simulation, the PAC for the non-CAR (chemically amplified resist) and the photo acid generator (PAG) for the CAR are calculated by Dill's model. In the delay model, the input parameter such as delay time affects the PAC or the PAG. For the post exposure bake (PEB) model, the modified PAC or PAG is calculated by solving diffusion equation due to input parameters such as time, temperature, and diffusion length. In the development model, the dissolution rate is calculated by using the dissolution theory. Resist profile is shown by using the ray tracing algorithm. Etch simulation shows the impact

of the final resist profile shape on the quality of the etched pattern in the substrate by using the Hamilton-Jacobi equation of the higher dimensional function. LAVA (the Lithography Analysis using Virtual Access) [3], PROLITH (the Positive Resist Optical LITHography model) [4], and SOLID-C (the Simulation of Optical Lithography in three Dimensions for the personal Computer) [1] are the lithography simulators for the personal computer among the academic and commercial tools.

2.2 Softbake (SB)

SB is a thermal process before exposure. During SB, the occurrence of photo-chemical reactions depends largely on the diffusion ability of a photoactive compound in a photoresist, and the free volume content of a photoresisst significantly affects its lithographic properties. In terms of the process physics, since the solvent of the resist is evaporated, the thickness of the resist shrinks, and the refractive index and the density of the resist are changed. This process can be a combination of solvent evaporation, solvent diffusion, and polymer compaction. The solvent concentration $S(z)$ in the solvent evaporation-diffusion process is

$$\frac{dS(z)}{dt} = -k_{evap} \bullet S(z) \bullet \delta(z) + \nabla D_S \nabla S(z), \tag{1}$$

where k_{evap} is the evaporation rate constant and D_S is the solvent diffusion coefficient. The free volume of the polymer film is

$$v_f = (1 - \chi_S) \bullet v_g + \alpha \bullet (T - T_g) + \chi_S \bullet \beta\,, \tag{2}$$

where χ_S is the mass fraction of solvent, T_g is the glass transition temperature of the pure polymer, v_g is the free volume of the pure polymer at T_g, α is the differential thermal expansion coefficient above the T_g, and ρ is density-scaled fractional volume parameter. The solvent diffusivity is

$$D = D_o \exp\left(-B\left(\frac{1}{v_f} - \frac{1}{v_g}\right)\right), \quad v_f > v_g, \qquad D = D_o\,, \quad v_f < v_g\,, \tag{3}$$

where D_o is the diffusion coefficient at T_g and B is the free volume efficiency parameter. The refractive index of the resist is

$$\eta_{resist} = \left(1 - \sum_i \chi_i\right) \bullet \eta_{polymer} + \sum_i \chi_i \bullet \eta_i, \tag{4}$$

where $\eta_{polymer}$ is the refractive index of the resist polymer, χ_i is the fraction of the i-th resist component remaining after the softbake step, and η_i is the complex refractive index of the i-th component [5].

2.3 Post-exposure Bake (PEB)

A typical positive-type CAR is composed of a polymer resin, a photoacid generator (PAG), and a dissolution inhibitor. When the CAR is exposed to light, acid is generated by

conversion of the PAG. The acid concentration is related to the exposure dose through Dill's ABC parameters. During PEB, this initial acid derives the de-protection reaction with a thermal acid-catalyzed reaction that alters the development rate of the resist. Exposing the resist to deep ultraviolet (DUV) light generates acid from the PAG. During a subsequent PEB, the photogenerated acid catalyzes a thermally induced reaction that cleaves the dissolution inhibitor groups (protecting groups), rendering the reacted (deprotected) region soluble in the aqueous developer. Meanwhile, the acid diffuses from a high-dose region to a low-dose region, washing out standing waves and causing the reacted region to be larger than the initially exposed region. In addition, most CARs exhibit volume shrinkage after the PEB step due to desorption of volatile group byproducts that are created during the bake. The PAG concentration changes during exposure and has been described by

$$\frac{d[PAG]}{dt'} = -C[PAG]I \rightarrow [PAG] = [PAG]_o e^{-CIt'}, \tag{5}$$

$$[A]_{dose} = [PAG]_o - [PAG] = [PAG]_o\left(1 - e^{-CE}\right), \tag{6}$$

where A is the acid and exposure dose (E) is the multiplication of intensity (I) to exposure time (t'). The acid concentration changes during PEB and has been described by

$$\frac{d[A]}{dt} = -k_{loss} \bullet [A] - k_{quench} \bullet [A] \bullet [B] + \nabla \bullet (D_{acid} \nabla [A]), \tag{7}$$

$$\frac{d[B]}{dt} = -k_{quench} \bullet [A] \bullet [B], \tag{8}$$

$$\frac{d[M]}{dt} = -k_{amp} \bullet [M] \bullet [A]^n, \tag{9}$$

where M is the protecting group of the polymer resin, B is the base quencher, k_{amp} is the acid-catalyzed deprotection rate, k_{loss} is the acid loss reaction rate, k_{quench} is the acid neutralization rate, and t is the PEB time.
The acid diffusivity is

$$D_{acid} = D_0 \exp\left(\frac{\alpha M}{1+\beta M}\right), \quad D_0 = A_r \exp\left(-\frac{E_a}{RT}\right), \tag{10}$$

where α and β are constants, E_a is the thermolytic decomposition activation energy, A_r is the Arrhenius coefficient, and R is the Boltzmann constant.
Table I shows the simulated parameters of the 90-nm line and space pattern. 140-nm mask pattern is used for the profile of a 90-nm L/ S pattern after the development process.
Figure 2 shows simulation results for CDs for overbake of SB and PEB for isolated 94-nm line and 90-nm L/ S patterns. When the SB time is increased in Fig. 2 (a), the CD becomes larger, and then saturate. When the PEB time is increased in Fig. 2 (b), the CD decreases to below 40 nm. In the L/ S patterns, the underbake of SB and the overbake of PEB can be used for 45-nm pattern formation. In the active area of Fig. 2, the CD sensitivity of the PEB time (2.86 nm/ s) is larger than that of the SB time (0.26 nm/ s).

- **Mask Pattern**
  90 nm isolated Line and Space (L/S) pattern
- **Modeling Options**
  Image Calculation Model: Scalar
- **Stepper Parameters**
  Illumination: Convential-partially coherent
  Defocus: 0.0 μm, Wavelength: 193 nm
  Illumination Pupil Shape: Dipole(radius: 0.5, holesize: 0.3, angle: 45)
  Numerical Aperture (NA): 0.8, Aberrations: none
  Flare[%]: 0
- **Film Stack**
  Layer 1: 390-nm resist, refraction : 1.72 - j0.0
  Layer 2: 82-nm AR™19, refraction : 1.79 - j0.4
  Layer 3: Silicon, refraction : 6.522 - j2.705
- **Prebake Parameters**
  Temperature: 120°C
  Time: 60 s
- **Exposure Parameters**
  Exposure Dose: 15 mJ/cm^2
  A: 0.01 (1/μm), B: 0.5 (1/μm) , C: 0.03 cm^2/mJ
- **Post-Exposure Bake Parameters**
  Diffusion Length: 0.035 μm
  Temperature: 130 °C
  Time: 77 s, Q: 0.067
  k_{amp} (1/s): 0.75, k_{loss} (1/s): 2.3x10^{-5}
  Resist Type: Positive
  Exponent n: 2
  Resist thickness reduction parameter: alpha: 1.77, beta: 0.02
  Activation Energy E_2: 0 eV
- **Develop Parameters**
  Development Model: Enhanced notch model
  Time: 45 s,
  R_{min}: 2x10^{-5} nm/s R_{max}: 0.045 μm/s
  R_{Res}: 0.0187 n: 1.61 l: 9.84

Table I. Parameters of the 90 nm line and space pattern.

Although the CD sensitivity of thermal parameters can be different due to other process parameters, the CD sensitivity of the PEB temperature is larger than that of the PEB time in the simulation of the L/S patterns. Both CD sensitivities are larger when the target pattern size is smaller.

Figure 3 shows boundary movements of the acid and the inhibitor concentration due to the extended times of SB and PEB for an isolated 94-nm line pattern. Those resist bulk images are the distributions of acid concentration after exposure and inhibitor concentration after PEB at a SB time of 120 s in Figs. 3 (a) and (c) and at a SB time of 10 s in Figs. 3 (b) and (d).

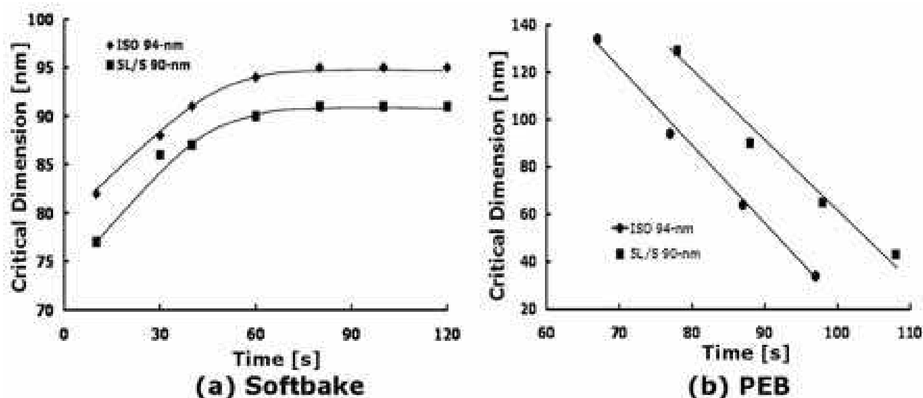

Fig. 2. Simulation results for the critical dimensions (a) SB and (b) PEB for isolated 94-nm line and 90-nm line and space (L/ S) patterns.

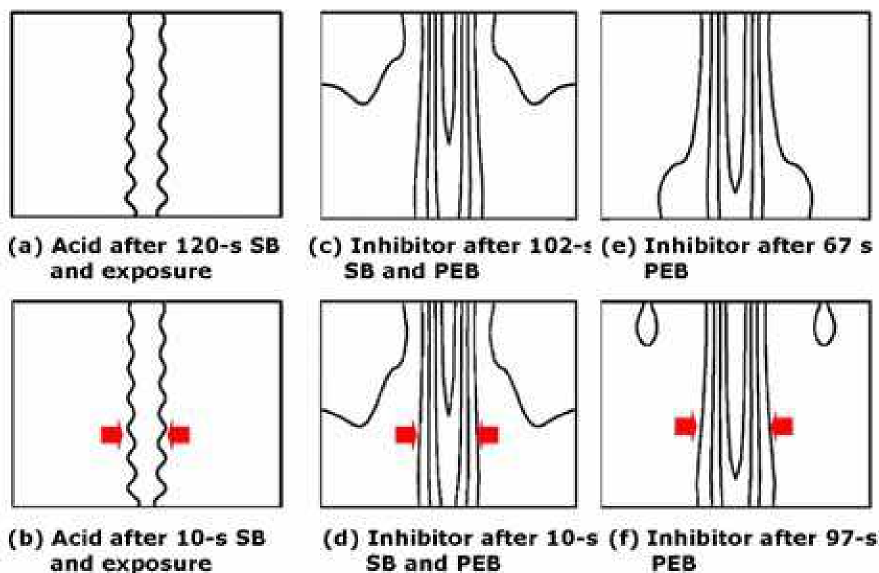

Fig. 3. Resist bulk images of (a) acid concentration after exposure and (c) inhibitor concentration after PEB at a SB time of 120 s, (b) the acid concentration after exposure and (d) inhibitor concentration after PEB at a SB time of 10 s, and inhibitor concentrations at PEB times of (e) 67 s and (f) 97 s.

Figures 3 (e) and (f) show inhibitor concentrations at PEB time of 67 s and 97 s, respectively. Figures (b), (d), and (f) for small patterns can be distinguished from Figs. (a), (c), and (e) for large patterns. Hence, for small pattern formation, the boundaries of acid and inhibitor concentrations move to the center of horizontal axis and become dense. A small SB time and a larger PEB time make the boundaries of the acid and the inhibitor concentrations dense at the center of the horizontal axis.

2.4 Thermal reflow process

Thermal reflow, as a resolution-enhancement technique, is a good method without any additional complex process steps and with appropriate selection of the resist properties and thermal loading process conditions. The thermal reflow process is used to reduce the pattern size of a resist by thermally heating the resist over its glass transition temperature after the development process. When the resist is heated over its glass transition temperature, the bonding of the synthesized resist is reduced and its mobility is improved. The three-dimensional structure of the synthesized resist is changed, and the contact hole (C/ H) pattern size is shrunk due to the additional thermal energy.

However, it is difficult to predict the results of thermal reflow and process optimization, one reason being the optical proximity (or process) effects (OPEs), such as the impact of the image distortion. The OPEs of thermal reflow becomes quite severe as the critical dimensions shrink down to sub-50 nm patterns. If the physics governing a particular OPE is known through experiment and simulation, the distortion can be predicted and modeled. Even when the physics that govern the systematic effects are not fully understood, it still could be modeled if sufficient simulated data are available. Although the simulation parameters are not used to analyze the chemical phenomena of thermal reflow, the critical dimension bias after resist reflow can be predicted in a linear system by using the fitting function of experimental data. Through the optical proximity correction (OPC), the distorted image can be manipulated back to the original designed image.

2.4.1 Boundary-movement method

Boundary movement represents the boundary as a geometric model and solves the partial differential equations for boundary motion. The level-set method is more accurate and efficient than the Lagrangian-type method. The level-set function $\psi(x,y,t)$ is defined as the distance of a point (x,y) to the boundary of the geometry under consideration. The point (x,y) in the geometry boundary is

$$\psi(x,y,t) = 0. \tag{11}$$

Assuming that each boundary point moves along its surface normal,

$$\frac{\partial \psi(x,y,t)}{\partial t} + V\left|\nabla \psi(x,y,t)\right| = 0, \tag{12}$$

where V is velocity (μm/ s) of movement. The basic equation system of fluid flow consists essentially of the continuity equation and the conservation equations of momentum and energy. Under the condition that fluid is incompressible and Newtonian, the continuity equation in two dimensions is

$$\frac{\partial v}{\partial x} + \frac{\partial u}{\partial y} = 0, \tag{13}$$

where v and u are the velocity components in the x and y directions, respectively. The conservation equations of momentum are

$$\rho\left(\frac{\partial v}{\partial t} + v\frac{\partial v}{\partial x} + u\frac{\partial v}{\partial y}\right) + \frac{\partial p}{\partial x} = \mu\left(\frac{\partial^2 v}{\partial x^2} + \frac{\partial^2 v}{\partial y^2}\right) + \rho g_x, \tag{14}$$

$$\rho\left(\frac{\partial u}{\partial t}+v\frac{\partial u}{\partial x}+u\frac{\partial u}{\partial y}\right)+\frac{\partial p}{\partial y}=\mu\left(\frac{\partial^2 u}{\partial x^2}+\frac{\partial^2 u}{\partial y^2}\right)+\rho g_y, \tag{15}$$

where p is pressure and ρ is density. The components of gravitational acceleration in the x and y directions are denoted by g_x and g_y, respectively. The symbol μ is fluid viscosity [kg/ m•s]. When the velocity component in the y-direction is negligibly small compared to that in the x-direction, from Eqs. (13) and (14)

$$\frac{\partial v}{\partial x}=0, \tag{16}$$

$$\rho\left(\frac{\partial v}{\partial t}\right)+\frac{\partial p}{\partial x}=\mu\left(\frac{\partial^2 v}{\partial x^2}\right)+\rho g_x. \tag{17}$$

If the gravitational acceleration g_x is negligible, then Eqs. (16) and (17) above can be approximated as

$$\rho\left(\frac{\partial v}{\partial t}\right)=\mu\left(\frac{\partial^2 v}{\partial x^2}\right). \tag{18}$$

If we assume that Eq. (18) is the standard diffusion equation, the thermal reflow length is

$$L=\sqrt{\frac{\mu}{\rho}t}. \tag{19}$$

The boundary point from Eq. (12) moves such that

$$\psi(x,y,t+\Delta t)=\psi(x,y,t)-L\left|\nabla\psi(x,y,t)\right|, \tag{20}$$

where the thermal reflow length (L) is $\Delta t \bullet v$, because the length can be represented as the product of velocity and time.

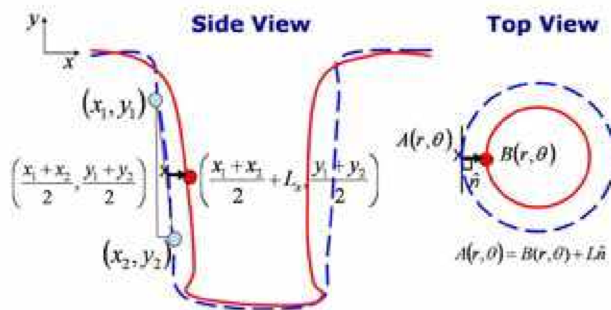

Fig. 4. Thermal flow length.

Figure 4 shows the movement of point (x_1, y_1) and point (x_2, y_2) using the thermal reflow length. After the midpoint of point (y_1, y_1) and point (y_2, y_2) is calculated, this midpoint is moved to thermal reflow length due to time and temperature.

Piecewise-linear	**Polynomial**
$\mu(T) = \mu_n + (\mu_{n+1} - \mu_n)/(T_{n+1} - T_n) * (T - T_n)$ (a)	$\mu(T) = A_1 + A_2 T + A_3 T^2 + \dots$ (e)
Piecewise-polynomial	**Sutherland's law**
For $T_{min,1} < T < T_{max,1}$ $\mu(T) = A_1 + A_2 T + A_3 T^2 + \dots$ (b)	$\mu(T) = C_1 T^{3/2}/(T - C_2)$ (f) or
For $T_{min,2} < T < T_{max,2}$ $\mu(T) = B_1 + B_2 T + B_3 T^2 + \dots$ (c)	$\mu(T) = \mu_0 (T/T_0)^{3/2} (T_0 + S)/(T + S)$ (g)
Power law	**Standard Arrhenius form (supposed)**
$\mu(T) = BT^n$ (g) or $\mu(T) = \mu_0 (T/T_0)^n$ (d)	$\mu(T) = \mu_0 \exp(E/(RT))$ (h)

Table II. Viscosities as a function of temperature.

Viscosity (μ) is related to the fluid's resistance to motion and is an important aspect of rheology. Viscosity is determined by relating the velocity gradient in fluids to the shear force causing flow to occur. To define the viscosity equation as a function of temperature, viscosity equations in Table II are fitted to the experiment data.

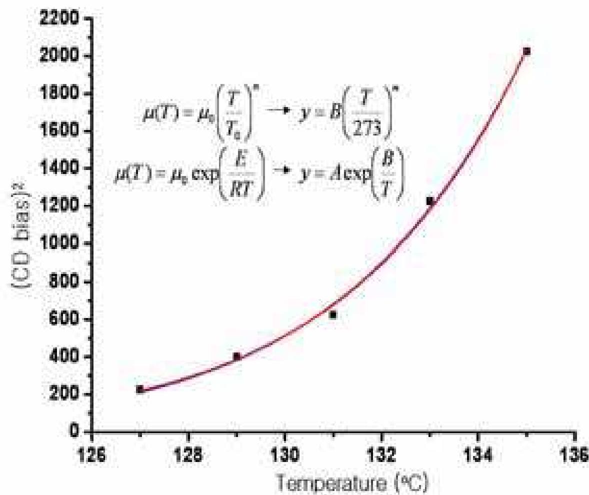

Fig. 5. Fitting experimental data by using viscosity equation of a function of temperature.

Figure 5 shows the experimental relation of temperature and the viscosity, which is from Eq. (19),

$$L^2 = \frac{t}{\rho}\mu \quad \rightarrow \quad \mu(T) \propto (CD\,bias)^2 \cdot \tag{21}$$

Two equations are fitted when A=3.0062×10^{14}, n=36.52117, A=7.5727×10^{18}, and B=-4840.2. Hence, two functions can be used as the viscosity function.
The function of viscosity can be

$$\mu(T) = \mu_0 \exp\left(\frac{E}{RT}\right), \tag{22}$$

- **Mask Pattern**
  140-nm × 140-nm isolated rectangle pattern
- **Modeling Options**
  Image Calculation Model: Scalar
- **Stepper Parameters**
  Illumination: Convential-partially coherent
  Defocus: 0.0-μm, Wavelength: 193-nm
  Illumination Pupil Shape: Dipole (radius: 0.5, hole size: 0.3, angle: 45°)
  Numerical Aperture (NA): 0.7, Aberrations: none
  Flare[%]: 0
- **Film Stack**
  Layer 1: 250-nm resist, refraction : 1.72 - j0.02
  Layer 2: 82-nm AR™19, refraction : 1.79 - j0.4
  Layer 3: Silicon, refraction : 6.522 - j2.705
- **Prebake Parameters**
  Temperature: 120°C
  Time: 60 s
- **Exposure Parameters**
  Exposure Dose: 19 mJ/ cm^2
  A: 0.01 (1/ μm), B: 0.08 (1/ μm), C: 0.02-cm^2/ mJ
- **Post-Exposure Bake Parameters**
  Diffusion Length: 0.035-μm
  Time: 80 s, Q: 0.067
  k_{amp} (1/ s): 0.75, k_{loss} (1/ s): 2.3×10^{-5}
  Resist Type: Positive
  Exponent n: 1
  Resist thickness reduction parameter: alpha: 1.74, beta: 0.02
  Activation Energy E_2: 0 eV
- **Develop Parameters** Development Model: Enhanced Mack
  Time: 150 s,
  R_{min}: 6.5×10^{-5}-nm/ s R_{max}: 0.1-μm/ s
  R_{Res}: 0.0187 n: 0.01 l: 0.73
- **Resist Reflow Parameters**
  Temperature: 129°C, Time: 90 s

Table III. Parameters of the 140-nm contact hole pattern after resist reflow.

where E is the activation energy, μ_o is the pre-exponential factor, and R is the universal gas constant. A fitted viscosity function, $\mu = (4.8414 \times 10^{16}) \bullet \exp(-4840.2 / T)$, is used for the simulation when the density is constant due to temperature.

Table III shows the simulated parameters of the 140-nm contact hole after resist flow. A 140-nm mask pattern is used for the profile of a 180-nm C/ H pattern after the development process. After the resist flow process of 129 °C for 90 seconds, the 180-nm developed profile is shrunk to the 140-nm resist profile.

Figure 6 shows the simulated and experimental resist profiles after resist flow at 129 °C and 90 seconds. The critical dimension bias is 40 nm. The bulk image of simulation modeled by Eqs

(21) and (22) is shown as similar to the experimental bulk image. Figure 6 shows the comparison of CDs and CD biases after resist flow at 90 seconds in experiment and simulation according to temperature. Our simulated results agree well with experimental results.

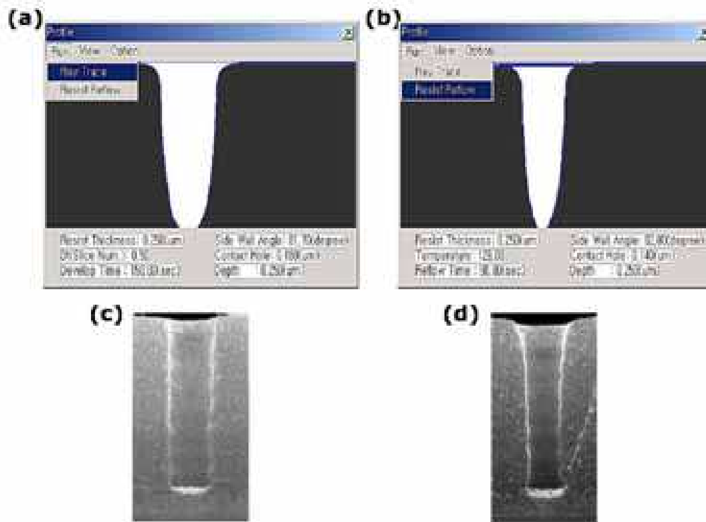

Fig. 6. Simulation results of (a) a 180-nm contact hole pattern before resist reflow, and (b) a 140-nm contact hole after resist reflow. Experimental results of (c) 180-nm contact hole pattern before resist reflow, and (d) 140-nm contact hole pattern after the resist reflow process.

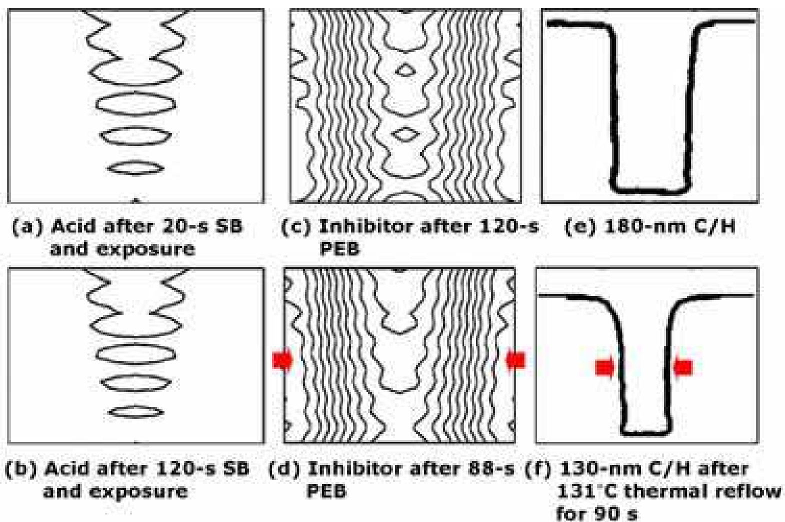

Fig. 7. Resist bulk images of acid concentration after exposure at SB times of (a) 20 s and (b) 120 s, inhibitor concentrations at PEB times of (c) 120 s and (d) 88 s, (e) the 180-nm contact hole before thermal reflow, and (f) the 130-nm contact hole after thermal reflow at 131 °C for 90 s.

Figure 7 shows boundary movements for a C/ H in SB, PEB, and thermal reflow. These resist bulk images are the distributions of acid concentrations after exposure at a SB time of 20 s in Fig. 7 (a) and at a SB time of 120 s in Fig. 7 (b). Figures 7 (c) and (d) show inhibitor concentrations at PEB times of 120 s and 88 s, respectively. Figures 7 (e) and (f) show the 180-nm C/ H before thermal reflow and the 130-nm C/ H after thermal reflow, respectively, at 131 °C for 90 s. For the extended SB time, the boundaries of the acid concentration are same in Figs. 7 (a) and (b), so the SB time is not sensitive to shrinkage of the contact hole. For the extended PEB time, the boundaries of the inhibitor concentration move to the center of the horizontal axis, and become dense. During the thermal reflow in Figs. 7 (e) and (f), the boundary of the C/ H shrinks due to temperature and time.

2.4.2 Solution of the Navier-Stokes equation

The resist reflow at temperature above its glass transition temperature can be assumed to be an ideal fluid, which is an incompressible fluid, and to have a constant density (ρ) and force ($\rho\hat{n}\delta S$) exerted across a geometrical surface element $\hat{n}\delta S$ within the fluid. Hence,

$$\frac{D\vec{u}}{Dt} = -\frac{1}{\rho}\nabla P + g \ , \ \ \nabla \bullet \vec{u} = 0 \, , \tag{23}$$

where $\vec{u}(u,\phi,w)$ is the fluid velocity, g is the gravitational acceleration, ρ is the density, and P is the pressure. At this point, the element of the stress tensor (T_{ij}) in an incompressible fluid is

$$T_{ij} = -p\delta_{ij} + \mu\left(\frac{\partial u_j}{\partial x_i} + \frac{\partial u_i}{\partial x_j}\right), \ \ \nabla \bullet \vec{u} = 0 \, . \tag{24}$$

where μ is fluid viscosity. By Eqs. (23) and (24),

$$\rho\frac{Du_i}{Dt} = -\frac{\partial P}{\partial x_i} + \mu\frac{\partial}{\partial x_j}\left(\frac{\partial u_j}{\partial x_i} + \frac{\partial u_i}{\partial x_j}\right) + \rho g_i \, , \tag{25}$$

$$\frac{Df}{Dt} = \frac{\partial f}{\partial t} + u\frac{\partial f}{\partial x} + v\frac{\partial f}{\partial y} + w\frac{\partial f}{\partial z} \rightarrow \frac{Df}{Dt} = \frac{\partial f}{\partial t} + (\vec{u} \bullet \nabla)f \, . \tag{26}$$

Hence, the Navier-Stokes equation is

$$\frac{\partial \vec{u}}{\partial t} + (\vec{u} \bullet \nabla)\vec{u} = -\frac{1}{\rho}\nabla P + v\nabla^2\vec{u} + g \, , \tag{27}$$

$$\nabla \bullet \vec{u} = 0 \, , \tag{28}$$

where $\nu = \mu/\rho$ is kintic viscosity. In the x and the z directions,

$$\rho\left(\frac{\partial u}{\partial t} + u\frac{\partial u}{\partial x} + w\frac{\partial u}{\partial z}\right) = -\frac{\partial P}{\partial x} + \mu\left(\frac{\partial^2}{\partial x^2} + \frac{\partial^2}{\partial z^2}\right)u + \rho g_x \, , \tag{29}$$

$$\rho\left(\frac{\partial w}{\partial t}+u\frac{\partial w}{\partial x}+w\frac{\partial w}{\partial z}\right)=-\frac{\partial P}{\partial z}+\mu\left(\frac{\partial^2}{\partial x^2}+\frac{\partial^2}{\partial z^2}\right)w+\rho g_z, \quad (30)$$

$$\frac{\partial u}{\partial x}+\frac{\partial w}{\partial z}=0\cdot \quad (31)$$

When $\vec{u}\bullet\nabla\vec{u}\langle\langle\mu\nabla^2\vec{u}$ for the slow flow equation and when the gravitational acceleration (g_x) and pressure are neglected, the Navier-Stokes equation becomes the diffusion equations

$$\frac{\partial H}{\partial t}=v\frac{\partial^2 H}{\partial x^2}, \quad \text{if } u\approx H(x,t), \quad (32)$$

where H is a geometric boundary. In the shallow-water approximation, the Navier-Stokes equation becomes

$$\frac{\partial u}{\partial t}+u\frac{\partial u}{\partial x}+w\frac{\partial u}{\partial z}=-\frac{1}{\rho}\frac{\partial P}{\partial x}, \quad (33)$$

$$\frac{\partial w}{\partial t}+u\frac{\partial w}{\partial x}+w\frac{\partial w}{\partial z}=-\frac{1}{\rho}\frac{\partial P}{\partial z}-g_z, \quad (34)$$

$$\frac{\partial u}{\partial x}+\frac{\partial w}{\partial z}=0\cdot \quad (35)$$

From Eq. (35),

$$w=-\frac{\partial u}{\partial x}z+f(x,t) \quad (36)$$

and $f(x,\ t)$ = 0 when w = 0 at z = 0. If $F(x,\ z,\ t)=z-H(x,\ t)$ in the kinematic condition at the free surface,

$$\frac{\partial F}{\partial t}+(\vec{u}\bullet\nabla)F=0, \text{ at } z=H(x,\ t). \quad (37)$$

From Eqs. (36) and (37),

$$\frac{\partial H}{\partial t}+u\frac{\partial H}{\partial x}+H\frac{\partial u}{\partial x}=0\cdot \quad (38)$$

By using $c(x,t)=(gH)^{\frac{1}{2}}$ and Eq. (33),

$$\left[\frac{\partial}{\partial t}+(u-c)\frac{\partial}{\partial x}\right](u-2c)=0\cdot \quad (39)$$

When $u+2c=2c_0$, $z=-3c+2c_0$, and $z\approx c\approx H(x,t)$,

$$\frac{\partial H}{\partial t}+H\frac{\partial H}{\partial x}=0\cdot \quad (40)$$

For an analytical solution, the gravitational acceleration (g_x) in the x-direction is zero and $\vec{u} \bullet \nabla \vec{u} \langle\langle \mu \nabla^2 \vec{u}$ for the slow flow equations. From Eq. (29),

$$0 = -\frac{1}{\rho}\frac{\partial P}{\partial x} + v\frac{\partial^2 u}{\partial z^2} \quad \text{for x-coordinate,} \tag{41}$$

where kinetic viscosity is $v = \mu/\rho$. From Eq. (30),

$$0 = -\frac{1}{\rho}\frac{\partial P}{\partial z} - g \quad \text{for z-coordinate.} \tag{42}$$

The net upward force per unit area of surface is, by Eq. (41),

$$P - P_0 = -\Im\frac{\partial^2 H}{\partial x^2} \rightarrow P = -\rho g H - \Im\frac{\partial^2 H}{\partial x^2}, \tag{43}$$

where P is the pressure in the fluid just below the surface, P_0 is the atmospheric pressure, and $\Im$ is the surface tension force. If the geometric boundary function (H) is a power series, $H = 1 + x + x^2 + \cdots$ and if x is smaller then 1, $H \approx 1 + x$ and

$$P = -\rho g(1 + x) - \Im\frac{\partial^2 H}{\partial x^2}. \tag{44}$$

From Eqs. (41) and (44),

$$u = -\left[\frac{g}{v}\frac{\partial H}{\partial x} + \frac{\Im}{v\rho}\frac{\partial^3 H}{\partial x^3}\right]\frac{1}{2}z^2. \tag{45}$$

From Eq. (31),

$$w_{z=H} = \frac{\partial}{\partial x}\left[\frac{g}{v}\frac{\partial H}{\partial x} + \frac{\Im}{v\rho}\frac{\partial^3 H}{\partial x^3}\right]\frac{1}{6}H^3. \tag{46}$$

The boundary condition is $F(x,z,t) = z - H(x,t) = 0$, so that

$$\frac{\partial H}{\partial t} = \frac{\partial}{\partial x}\left[\frac{H^3}{6}\left(\frac{g}{v} + \frac{\Im}{v\rho}\frac{\partial^3 H}{\partial x^3}\right)\right], \tag{47}$$

$$\frac{\partial H}{\partial \tau} = \frac{1}{6}\frac{\partial}{\partial X}\left[\Omega^{-2}\left(\frac{\partial^3 H}{\partial X^3}\right)H^3 + H^3\right], \; X \equiv \frac{x}{w}, \; \tau \equiv \frac{gt}{wv}, \; \Omega^2 \equiv \frac{\rho g w^3}{\Im}, \tag{48}$$

where H is the film geometry, w is the feature width, v is the kinematic viscosity of the fluid, and $\Im$ is the surface tension. A quasi-steady state of resist reflow can be obtained by dropping $\partial H/\partial\tau$ from Eq. (48):

$$\left(\frac{\partial^3 H}{\partial X^3}\right)H^3 + \Omega^2 H^3 = \Omega^2. \tag{49}$$

Analytical solutions with the dimensionless parameter (Ω^2) can be obtained. In the isolated contact hole, the entire domain can be divided into subdomain I of the left ridge side, subdomain II of the inside ridge, and subdomain III of the right ridge side. The film geometries are

$$H_I = 1 + b_1\phi_2 + c_1\phi_3, \quad H_{II} = 1 \pm \frac{d}{1+\Omega^2} + a_2\phi_1 + b_2\phi_2 + c_2\phi_3 + \phi_4, \quad H_{III} = 1 + a_3\phi_1, \tag{50}$$

where a, b, and c are coefficients, which are calculated by using the boundary conditions, d is the height of resist, and ϕ is the linearly independent homogenous solutions. The three linear independent homogenous solutions are

$$\phi_1 = \exp(-\lambda x), \quad \phi_2 = \exp(\lambda x/2)\cos(\lambda x\sqrt{3}/2),$$

$$\phi_3 = \exp(\lambda x/2)\sin(\lambda x\sqrt{3}/2), \quad \phi_4 = \frac{1}{3}\left[\left(1 \pm \frac{d}{1+\Omega^2}\right) - \left(1 \pm \frac{d}{1+\Omega^2}\right)^4\right], \tag{51}$$

where in subdomains I and III, $\lambda = (3\Omega^2)^{1/3}$ and , in subdomain II, $\lambda = \{3\Omega^2\{1 \pm d/(1+\Omega^2)\}^{-4}\}^{1/3}$. In the boundary condition of x = -1/ 2,

$$H_I \pm d = H_{II}, \quad \frac{\partial H_I}{\partial X} = \frac{\partial H_{II}}{\partial X}, \quad \frac{\partial^2 H_I}{\partial X^2} = \frac{\partial^2 H_{II}}{\partial X^2}. \tag{52}$$

In the boundary condition of x = 1/ 2,

$$H_{III} \pm d = H_{II}, \quad \frac{\partial H_{III}}{\partial X} = \frac{\partial H_{II}}{\partial X}, \quad \frac{\partial^2 H_{III}}{\partial X^2} = \frac{\partial^2 H_{II}}{\partial X^2}. \tag{53}$$

If wafer has a topology, the thickness of resist after thermal reflow is different due to reflow conditions. The surface tension of resist varies due to the non-uniformity of resist thickness. In the dense contact holes, the film geometries are

$$H_I = 1 + \frac{d}{1+\Omega^2} + a_2\phi_1 + b_2\phi_2 + c_2\phi_3 + \phi_4, \tag{54}$$

$$H_{II} = 1 + a_2\phi_1 + b_2\phi_2 + c_2\phi_3. \tag{55}$$

The boundary conditions at x = 1/ 2 are

$$H_I = H_{II} + d, \quad \frac{\partial H_I}{\partial X} = \frac{\partial H_{II}}{\partial X}, \quad \frac{\partial^2 H_I}{\partial X^2} = \frac{\partial^2 H_{II}}{\partial X^2}. \tag{56}$$

The boundary conditions between x = - 1/ 2 and x = a + 1/ 2 are

$$H_{II(X=z+1/2)} + d = H_{I(X=-1/2)}, \quad \frac{\partial H_I}{\partial X_{(X=-1/2)}} = \frac{\partial H_{II}}{\partial X_{(X=a+1/2)}}, \quad \frac{\partial^2 H_I}{\partial X^2_{X=-1/2}} = \frac{\partial^2 H_{II}}{\partial X^2_{(X=a+1/2)}}. \tag{57}$$

Figure 8 shows the numerical result of the diffusion equation in Eq. (32). The isolated pattern is wide and symmetrical due to the time of thermal reflow. The numerical

calculation methods are the second predictor-corrector scheme, quick scheme, the forward time and centered space (FTCS) scheme, and the Kawamara-Kuwahara scheme.

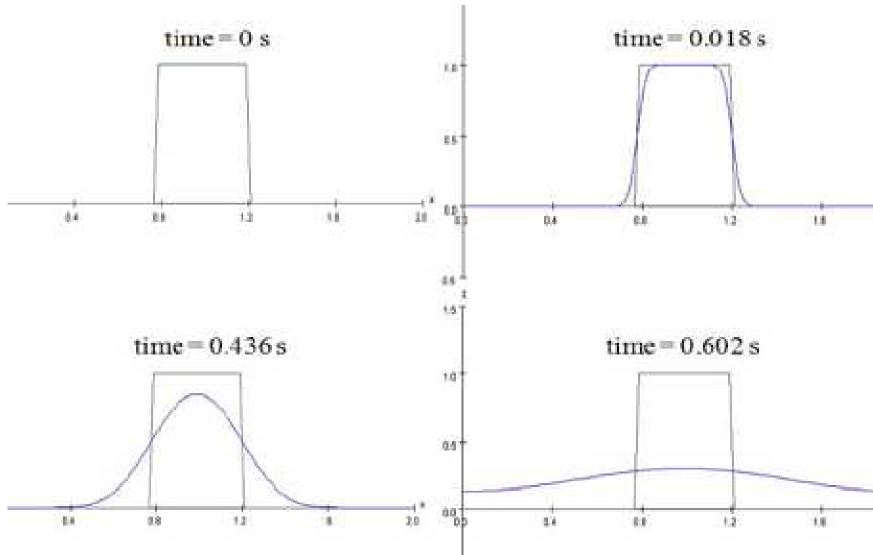

Fig. 8. Simulation results of the diffusion equation in Eq. (32) by using are the second predictor-corrector scheme, quick scheme. The isolated pattern is wider and symmetrical due to the time of thermal reflow.

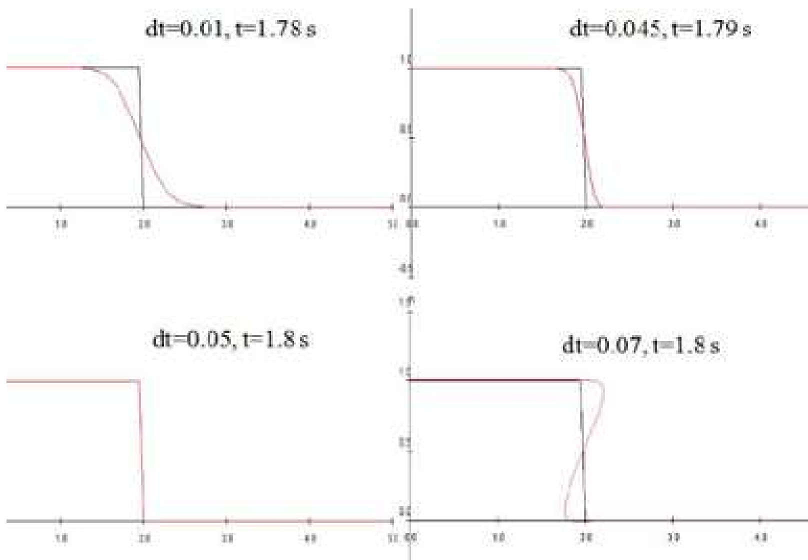

Fig. 9. Simulation flow of Eq. (40) due to Δt of the courant number, which is reflow time interval.

Thank You for previewing this eBook

You can read the full version of this eBook in different formats:

- HTML (Free /Available to everyone)
- PDF / TXT (Available to V.I.P. members. Free Standard members can access up to 5 PDF/TXT eBooks per month each month)
- Epub & Mobipocket (Exclusive to V.I.P. members)

To download this full book, simply select the format you desire below